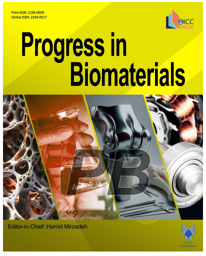

Volume 14, Issue 1, 142505 (1-20)

Progress in Biomaterials (PIBM)

https://doi.org/10.57647/pibm.2025.142505

Preparation and Assessment of Polyurethane-Polygycerol Itaconate-ZnO Composite as Guided Bone Regeneration Scaffold

Mahdiyeh Naseripour[1], Tahmineh Ahmadi[1,*], Shahrokh Shojaei[1,*], Salar Mohammadi Shabestari[2], Vahabodin Goodarzi[3]

[1] *Department of Biomedical Engineering, Islamic Azad University, Central Tehran Branch, Tehran, Iran.*
[2] *Department of Polymer, School of Chemical Engineering, College of Engineering, University of Tehran, Tehran, Iran.*
[3] *Tissue Engineering and Regenerative Medicine Research Center, Baqiyatallah University of Medical Sciences, Tehran, Iran.*

[*] **Corresponding authors:** tahmadi56@yahoo.com, and shahrokh.shojaei@gmail.com

Original Research

Received:
9 January 2025
Revised:
28 February 2025
Accepted:
16 March 2025
Published in issue:
31 March 2025

Abstract:

In this study, porous scaffolds for bone tissue engineering based on polyurethane and poly-glycerol-itaconic acid were fabricated using a salt-leaching method and reinforced with zinc oxide (ZnO) nanoparticles at 0, 5, and 10 wt.%. The resulting scaffolds were characterized by X-ray diffraction (XRD), elemental analysis (EDS/MAP), and Fourier-transform infrared spectroscopy (FTIR), confirming the successful incorporation of ZnO within the scaffold structure. Microstructural analysis revealed that the average pore sizes of scaffolds without ZnO and with 5 and 10 wt.% ZnO were 132 ± 92, 112 ± 58, and 92 ± 36 μm, respectively. Contact angle measurements indicated high hydrophilicity of the pure scaffold (6.9°) and a gradual increase in hydrophobicity with ZnO addition. Water absorption and degradation tests showed that the scaffold containing 10 wt.% ZnO exhibited the lowest equilibrium water uptake and improved control over degradation rate. Furthermore, antibacterial assays demonstrated that increasing ZnO concentration enhanced both bacteriostatic and bactericidal properties. Biocompatibility and cell adhesion assessments indicated that all scaffolds supported cellular attachment, with the 5 wt.% ZnO scaffold showing the most favorable biological performance, whereas the 10 wt.% ZnO scaffold exhibited significant cytotoxicity. Overall, the results indicate that polyurethane–poly-glycerol-itaconic acid scaffolds reinforced with 5 wt.% ZnO nanoparticles provide an optimal combination of structural integrity, biocompatibility, and antibacterial activity, making them a promising platform for guided bone regeneration and novel applications in dentistry and orthopedics.

Keywords: Polyurethane; Polyglycero itaconic acid; Zinc oxide; Scaffold; Bone tissue engineering

Cite this article: Naseripour, M., Ahmadi, T., Shojaei, S., Mohammadi Shabestari , S., Goodarzi, V., Preparation and Assessment of Polyurethane-Polygycerol Itaconate-ZnO Composite as Guided Bone Regeneration Scaffold. *Progress in Biomaterials* **14**(1), Article 05 (2025).

1. Introduction

Biomaterials are substances of natural or synthetic origin that are primarily used to improve, treat, repair, or replace tissues in living organisms. These materials must demonstrate sufficient biocompatibility and durability, while avoiding any adverse effects on surrounding tissues or interference with normal metabolic processes. Biomaterials can be obtained from natural sources or synthesized in laboratories through various techniques. The main classes of biomaterials used in the medical field include polymers, metallic–ceramic materials, and composites [1]. Guided bone regeneration (GBR), which utilizes barrier membranes, is recognized as one of the most effective approaches for alveolar bone reconstruction and the treatment of peri-implant bone defects [2]. Membranes play a crucial role in GBR success, as they prevent the migration of rapidly proliferating epithelial and connective tissues. This selective barrier creates adequate space for osteogenic cells and supports proper bone regeneration. However, the requirement for secondary surgery to remove non-degradable membranes can potentially harm newly formed tissues. To overcome this limitation, numerous studies have investigated the use of bioresorbable membranes [3]. Polymers have attracted increasing attention in scaffold fabrication for tissue engineering due to their broad range of mechanical properties, excellent biocompatibility, ease of processing, tunable characteristics, and flexibility [4].

Among natural polymers, collagen-based membranes are widely used because of their strong tissue integration ability. Nevertheless, their uncontrolled degradation rate and risk of disease transmission are major disadvantages [5]. As a result, synthetic polymers with adjustable physical and chemical properties have become increasingly attractive [6]. Some synthetic polymers, such as polycaprolactone (PCL), polyurethane (PU), and polylactic acid (PLA), offer easier processing and superior mechanical performance compared with natural polymers [2]. These advantages have led to the extensive application of biocomposite scaffolds in tissue engineering [7]. One of the most common methods for fabricating porous scaffolds is the salt-leaching technique. In this method, salt crystals act as porogens and are embedded within a mold, followed by the addition of a polymer solution and subsequent polymerization. The salt crystals are then removed using a solvent, leaving behind a porous polymeric scaffold. The pore size of the scaffold is directly related to the size of the salt particles, and both porosity and pore dimensions can be controlled by adjusting the amount and particle size of the salt used [8]. Zeytuni et al. [9] fabricated microporous polyvinylidene fluoride (PVDF) membranes using the salt-leaching technique, where sodium bicarbonate ($NaHCO_3$) served as the porogen. The membrane porosity was controlled by adjusting the amount of salt. Similarly, Correia et al. [10] produced piezoelectric PVDF scaffolds through the solvent casting/salt leaching method, using sodium chloride (NaCl) as the porogen and distilled water as the solvent. The resulting scaffolds exhibited pore sizes ranging from 300 to 400 µm.

In another study, Bera et al. [11] developed porous PVDF/PFC composites using solvent casting and salt leaching, with NaCl as the porogen. After drying, the salt was removed by washing with water. Likewise, prepared PMMA–PVDF nanocomposite foams via solvent casting and salt leaching, employing NaCl as the porogen and distilled water as the solvent to generate a porous nanostructure.

In the present study, synthetic polymers—polyurethane (PU) and polyglycero itaconate (PGIt)—with and without zinc oxide (ZnO) nanoparticles were used to fabricate porous scaffolds through the salt-leaching technique. The microstructure, biocompatibility, biodegradability, and cytotoxicity of the prepared scaffolds were systematically examined using appropriate characterization methods.

In recent years, guided bone regeneration (GBR) has gained significant attention as an effective approach in bone tissue engineering. In this technique, polymeric membranes act as physical barriers that prevent soft tissue ingrowth while providing favorable conditions for osteoblast differentiation and bone tissue formation [12].

The selection of a suitable scaffold material plays a crucial role in the overall success of the process. Synthetic polymers such as polycaprolactone (PCL), polylactic acid (PLA), and the PLGA copolymer are widely used because of their controlled degradation rates and high mechanical strength. For example, Lee et al. [13] reported that a 3D-printed PCL/β-TCP scaffold significantly enhanced new bone formation in an animal model. Similarly, Park et al. [14] demonstrated that the addition of hydroxyapatite nanoparticles to PLGA increased the expression of osteogenic genes such as Runx2 and OCN.

In addition to synthetic materials, natural polymers such as chitosan, gelatin, and collagen are widely used due to their excellent biocompatibility. Zhou et al. [15] showed that a chitosan/collagen scaffold containing BMP-2 enhanced bone regeneration by 2.5-fold compared with the control group. Likewise, Wang et al. [16] investigated a gelatin methacrylate (GelMA) scaffold containing bioceramic particles, which led to increased bone density in a rat model.

Recent research has shifted toward the development of hybrid and smart scaffolds. Kim et al. [17] designed a PCL/-chitosan/hydroxyapatite scaffold with high porosity that achieved 72% defect filling with new bone after eight weeks *in vivo*. Moreover, Liu et al. [18] proposed oxygen- and pH-responsive scaffolds for the controlled release of growth factors, promoting simultaneous angiogenesis and osteogenesis. Overall, combining synthetic and natural polymers, incorporating inorganic nanoparticles, and embedding growth factors represent effective strategies for improving bone regeneration in GBR applications.

Polyurethane (PU) serves as the elastomeric phase within the scaffold structure, enhancing its compressive and tensile strength. The soft and flexible nature of PU allows the scaffold to withstand the mechanical stresses of the bone environment without fracture [19]. Additionally, the urethane groups in the polymer chain improve interfacial adhesion between the polymer matrix and ZnO nanoparticles, leading to an increased Young's modulus and enhanced mechanical durability [20].

Polyglycero itaconate (PGItc) functions as the biodegradable phase, gradually degrading under physiological conditions through its carboxylic groups. This controlled degradation releases non-toxic byproducts and facilitates the replacement of the scaffold with newly formed bone tissue [21]. Moreover, PGItc enhances surface hydrophilicity, promoting protein adsorption and cell adhesion [22].

Although the potential clinical applications of this composite will be discussed in detail in the "Discussion and Conclusion" section, it is worth noting here that such structures have potential use in jawbone defect repair, peri-implant bone regeneration, and long-bone tissue engineering [17].

2. Materials and methods

2.1 Materials

In this study, polyurethane, itaconic acid, zinc oxide (ZnO) nanoparticles, dimethyl sulfoxide (DMSO), polytetramethylene ether glycol, and 1,4-butanediol were purchased from

Sigma-Aldrich. Glyceride, dioxane, dimethylformamide (DMF), hexamethylene diisocyanate, and stannous octoate were obtained from Aldrich. Zinc oxide (ZnO) was selected because of its unique combination of antibacterial activity, biocompatibility, and uniform dispersibility within polymeric matrices. Its antibacterial effect primarily results from the generation of reactive oxygen species (ROS) and the release of Zn^{2+} ions, which exhibit strong antimicrobial activity against both Gram-positive and Gram-negative bacteria. In biological environments, Zn^{2+} ions also promote osteoblast proliferation and differentiation while inhibiting osteoclast activity, processes that are essential for effective bone regeneration. Furthermore, the homogeneous distribution of ZnO nanoparticles within the polymer matrix prevents particle agglomeration, improves the mechanical stability of the scaffold, and maintains its biological functionality [23].

The incorporation of ZnO nanoparticles into the scaffold structure enhances its overall performance in multiple ways. On one hand, these nanoparticles strengthen the interfacial interactions between polyurethane (PU) and polyglycero itaconate (PGItc), thereby improving interfacial adhesion and increasing the tensile strength of the scaffold [24]. On the other hand, the antibacterial properties of ZnO, combined with its ability to induce osteoblastic differentiation, accelerate the bone formation process under biological conditions [25]. Moreover, ZnO provides surface-active sites and facilitates the controlled release of bioactive ions, which enhance the surface hydrophilicity and contribute to improved biocompatibility of the scaffold [26].

2.1.1 Specific features of the composite for bone regeneration

The polyurethane–polyglycero itaconate–ZnO composite exhibits several key characteristics that make it highly suitable for bone regeneration. First, the scaffold possesses a well-distributed porous structure, which facilitates nutrient diffusion and osteoblast proliferation, thereby promoting the formation of new bone tissue [27]. Second, its high biocompatibility ensures better host integration and minimizes undesirable inflammatory responses [28]. Third, the scaffold demonstrates balanced water absorption, allowing for the controlled release of bioactive molecules or therapeutic agents and accelerating the overall healing process [29]. Finally, the uniform dispersion of ZnO nanoparticles within the scaffold enhances its antibacterial performance, reduces the risk of implant-site infection, and simultaneously improves mechanical stability.

2.2 Synthesis of three-dimensional scaffolds

2.2.1 Synthesis of Polyglycero Itaconate (PGItc)

Equimolar amounts of glyceride and itaconic acid were introduced into a chemical reactor and heated in an oil bath at 120 °C until a homogeneous mixture was obtained. During the reaction, water produced as a byproduct was continuously removed from the system using a vacuum pump to drive the esterification process to completion.

2.2.2 Synthesis of polyurethane (PU)

Polyurethane was synthesized by reacting two moles of hexamethylene diisocyanate (HDI) with three moles of polytetramethylene ether glycol (PTMEG) in a reactor maintained at 50 °C under a nitrogen atmosphere for 24 h. The temperature was then increased to 80 °C, and mixing continued for an additional 2 h. Subsequently, 1,4-butanediol was added dropwise, and the reaction was allowed to proceed at 80 °C for 72 h to complete polymerization.

2.2.3 Preparation of Composite Scaffolds

For composite fabrication, 70 wt.% polyglycero itaconate and 30 wt.% polyurethane were dissolved in a mixture of dioxane and dimethylformamide (DMF) and stirred at 70 °C for 24 h to obtain a uniform solution. Hexamethylene diisocyanate, stannous octoate ($Sn(Oct)_2$) as a catalyst, and sodium chloride (NaCl) as a porogen were then added. The solution was cast into a mold and dried, after which the salt was leached out using water, resulting in a highly porous scaffold.

2.2.4 Fabrication of ZnO-containing scaffolds

For ZnO-modified samples, ZnO nanoparticles were first dispersed in dioxane and dimethyl sulfoxide (DMSO) and sonicated for 5 min to ensure uniform dispersion. Subsequently, polyglycero itaconate and polyurethane were added to the suspension, and the mixture was stirred at 80 °C for 24 h. The subsequent casting and salt-leaching steps were identical to those used for the neat samples.

2.2.5 The resulting scaffolds were labeled as follows

-S1: Scaffold without ZnO
-S2: Scaffold containing 5 wt.% ZnO
-S3: Scaffold containing 10 wt.% ZnO

During the composite preparation process, the main challenge was achieving a uniform distribution of ZnO nanoparticles within the polymeric network. Due to their strong tendency to agglomerate, ZnO particles can weaken the mechanical properties of the scaffold and cause surface heterogeneity. To overcome this issue, ultrasonication was applied for 5 minutes, and polar solvents such as DMSO and DMF were used to stabilize the ZnO suspension [30]. In addition, precise control of the stirring speed and reaction temperature during the polymerization stage prevented possible nanoparticle degradation and undesirable alterations in the chemical structure of the polymer matrix [31]. Another challenge, the uniform control of scaffold porosity, was addressed by carefully adjusting the particle size and weight percentage of NaCl used as the porogen [32]. These optimization steps ensured the formation of a homogeneous porous structure while maintaining the mechanical integrity and biological performance of the scaffold.

2.3 Methods and characterization techniques

A comprehensive set of characterization techniques was employed to evaluate the polyurethane–polyglycero itaconic acid nanocomposites containing ZnO.

2.3.1 Chemical and structural analysis

Fourier-transform infrared spectroscopy (FTIR) was used to identify functional groups and chemical bonds, while X-ray diffraction (XRD) was applied to determine crystallinity and crystallite size [33]. FTIR spectra were recorded in the $400-4000$ cm^{-1} wavenumber range using a Thermo AVATAR device (USA). XRD measurements were performed with a PHILIPS PW1730 diffractometer (Netherlands) under the following conditions: step size = 0.05°, time per step = 1 s, Cu Kα X-ray wavelength = 1.54056 Å, voltage = 40 kV, and current = 30 mA, in the $10-50°$ 2θ range.

2.3.2 Morphological and elemental analysis

The surface morphology and nanoparticle distribution were examined using scanning electron microscopy (SEM/FE-SEM), while elemental composition and mapping were analyzed with EDX [34]. A Quanta 450 SEM (FEI, USA) was used for microstructural observations.

2.3.3 Surface and physical properties

Surface wettability was assessed by contact angle measurements using a JIKAN GAG-20SE device (Iran). Equilibrium water absorption and swelling tests were performed to evaluate the physical properties of the scaffolds [35]. Optical absorbance was measured at 600 nm using an ELISA reader (elx800, Biotek).

2.3.4 Biological evaluation

Antibacterial activity was assessed using minimum inhibitory concentration (MIC) and minimum bactericidal concentration (MBC) tests [36]. Cytotoxicity was evaluated using the Methyl Thiazolyl Tetrazolium (MTT) assay [13].

2.3.5 Instrumentation summary

-SEM/FESEM: Quanta 450 (FEI, USA)
-FTIR: Thermo AVATAR (USA)
-XRD: PHILIPS PW1730 (Netherlands)
-Contact Angle: JIKAN GAG-20SE (Iran)
-EDX Analysis: TESCAN VEGA-MIRA II and MIRA III (Czech Republic)

To evaluate the effectiveness of the scaffolds in bone regeneration, several key assays were performed. First, the cellular biocompatibility of the scaffolds was assessed using the MTT assay to determine the viability of L929 cells on the scaffold surfaces, providing an indicator of cytotoxicity and cellular acceptance [35]. Second, the antibacterial activity was evaluated through minimum inhibitory concentration (MIC) and minimum bactericidal concentration (MBC) tests, assessing the scaffold's ability to inhibit the growth of Gram-positive and Gram-negative bacteria [25]. Third, surface analyses using SEM and EDX were conducted to examine morphology and elemental composition, confirming the uniform distribution of nanoparticles and porosity within the scaffolds [24]. Finally, contact angle measurements and water absorption tests were performed to assess surface hydrophilicity and surface behavior, which are critical for facilitating cell adhesion [26].

For water uptake measurements, scaffold specimens (1×1 cm^2) were immersed in 10 mL phosphate-buffered saline (PBS) inside Falcon tubes and incubated at 37 °C. At predetermined time intervals, samples were removed, surface-dried with filter paper, and weighed. The percentage of weight change after 24 h was calculated by comparing the dry weight (W_d) with the swollen weight (W_s) using equation (1). Each measurement was repeated three times to ensure accuracy.

$$\text{EWA}(\%) = \frac{W_s - W_d}{W_d} \times 100 \tag{1}$$

The antibacterial effect of ZnO nanoparticles was evaluated against *Escherichia coli* (Gram-negative) and *Staphylococcus aureus* (Gram-positive). Scaffold samples (1×1 cm^2) were weighed, immersed in 1 mL of sterile PBS, and incubated at 37 °C for one week. Bacterial strains were initially cultured for 24 h at 37 °C on Mueller–Hinton agar plates and subsequently transferred to liquid Mueller–Hinton medium. A 0.5 McFarland standard suspension was prepared for each strain. Bacterial cultures without scaffold extract served as positive controls, while culture medium without bacteria served as negative controls.

Nine serial dilutions of the scaffold extract, along with the control groups, were dispensed into a 96-well plate and incubated for 24 h at 37 °C. Following incubation, the plates were imaged, and optical density was measured at 600 nm using an ELISA reader. To prevent interference with the readings, 1 µL of resazurin solution (6.75 mg/mL) was added to each well. Fluorescence was recorded at an excitation wavelength of 550 nm and an emission wavelength of 590 nm, where the fluorescence intensity was directly proportional to the number of viable bacteria in the wells.

The effect of ZnO nanoparticles on the adhesion and survival of mouse fibroblast (L929) cells was also investigated. Fibroblasts were cultured in DMEM supplemented with 10% fetal bovine serum (FBS) and 5% penicillin–streptomycin in flasks under standard culture conditions. Scaffold specimens (1×1 cm^2) were placed into wells of a 24-well plate. Cells were trypsinized, counted using a Neubauer chamber, and approximately 50,000 cells were seeded onto each scaffold. After 24 h of culture, non-adherent cells were removed by washing twice with PBS. The scaffold samples were then fixed with 2.5% paraformaldehyde for 20 min under a chemical hood. Subsequently, each specimen was dehydrated sequentially in 90%, 40%, and 20% ethanol solutions to prepare for further analysis.

2.4 Cell culture

To evaluate the biocompatibility of the scaffolds, the mouse fibroblast cell line L929 was used, which is compatible with DMEM High Glucose medium (Gibco). The complete culture medium consisted of 10% fetal bovine serum (FBS, Gibco) and 1% antibiotic solution containing penicillin (100 µg/mL) and streptomycin (100 µg/mL) (BioIdea, Iran). The culture medium was replaced every $2-3$ days depending on the growth rate, cell density, and color change of the medium. Cells were maintained in a cell culture incubator at 37 °C with 5% CO$_2$ under standard culture conditions.

2.5 Preparation of Phosphate-Buffered Saline (PBS)

To prepare 1 L of PBS solution, 8.5 g NaCl, 0.6 g KH_2PO_4, and 0.4 g Na_2HPO_4 were dissolved in distilled water. The pH was adjusted to 7.2 using a pH meter, and the solution was subsequently sterilized.

2.6 Extraction

Scaffold coupons (1×1 cm^2) were immersed in 1 mL PBS and incubated at 37 °C for 7 days. Since the extraction duration was relatively long and the scaffolds were non-sterile, PBS was used instead of culture medium to prevent bacterial growth and unwanted contamination.

2.7 MTT assay

To assess cell viability, 5,000 L929 cells per well were seeded into 96-well plates. Each experiment was performed in triplicate, including untreated cells as controls and complete medium without cells as blanks. After 24 h of incubation, the designated treatments were applied.

At the end of the treatment period, the medium was removed, and 100 µL of MTT solution (0.5 mg/mL) prepared in serum-free medium was added to each well. The plate was covered with aluminum foil and incubated for 3 h. Following incubation, the supernatant was gently removed, and 100 µL of DMSO was added to dissolve the formazan crystals formed by viable cells. The plate was again covered with foil and placed on a shaker at 200 rpm for 20 min.

Optical absorbance was measured at 600 nm using an ELISA reader (elx800, Biotek). Data analysis was performed by comparing treated samples with controls and blanks, and standard deviations were calculated for each group.The percentage of viable cells was calculated according to equation (2):

$$\text{Percentage of viable cells} = \frac{\text{A sample} - \text{A blank}}{\text{A control} - \text{A blank}} \times 100 \tag{2}$$

Normalization and graph plotting were performed using GraphPad Prism 9.0 software. Subsequently, paired t-tests ($p < 0.05$) were conducted to determine the statistical significance of each sample compared with the control.

2.8 Cell treatment

Volumes of 2.5, 5, 10, 20, and 40 µL of each extract were added to the wells containing cells. To maintain consistent culture conditions and compensate for volume differences, the 2.5, 5, 10, and 20 µL treatments were adjusted to 40 µL using PBS. The control group received 40 µL of sterile PBS without extract.

2.9 Table of abbreviations

Row	Full Name	Abbreviation
1	Polyurethane	PU or PUR
2	Glyceride	*
3	Itaconic Acid	IA
4	Zinc Oxide	ZnO
5	Dimethylformamide	DMF
6	Dimethyl Sulfoxide	DMSO
7	Dimethyl Sulfoxide	HDI
8	Polytetramethylene Ether Glycol	PTMEG
9	1,4-Butanediol	BDO
10	Tin(II) Octoate	$Sn(Oct)_2$
11	Fourier-Transform Infrared Spectroscopy	FTIR
12	X-Ray Diffraction	XRD
13	Scanning Electron Microscopy / Energy-Dispersive X-ray Spectroscopy	SEM/EDS
14	(3-(4,5-Dimethylthiazol-2-yl)-2,5-Diphenyltetrazolium Bromide)	MTT
15	Minimum Inhibitory Concentration / Minimum Bactericidal Concentration	MIC/MBC
16	Phosphate-Buffered Saline	PBS
17	Poly(glyconic acid-co-itaconic acid)	PGIt
18	Cell Contact Angle	CA
19	Cytotoxicity Assay	CTA

3. Results and discussion

3.1 XRD analysis

To investigate the crystalline structures, X-ray diffraction (XRD) analysis was utilized and the obtained diffraction patterns are illustrated in figure 1.

According to the XRD pattern of sample S1 (without zinc oxide nanoparticles), a broad diffraction peak is observed in the $15-30°$ (2θ) range, confirming the amorphous (non-crystalline) nature of the organic composite. Similar broad peaks have been reported in previous studies for organic-based composites [37]. In contrast, the samples containing ZnO nanoparticles display several sharp and well-defined peaks, indicating the formation of crystalline structures within the nanocomposites. The diffraction patterns were analyzed using HighScore Plus X'Pert software to identify the corresponding crystalline phases. As illustrated in figure 1, the XRD patterns of the samples containing 5 wt.% and 10 wt.% ZnO closely match the reference card JCPDS No. 01-079-2205 [16], which corresponds to hexagonal ZnO with a P63mc space group. The characteristic diffraction planes of ZnO, namely (100), (002), (101), and (102), appear at 31.2°, 32.9°, 35.1°, and 45.9°, respectively. The higher peak intensities observed in sample S3 confirm a greater concentration of ZnO nanoparticles within this nanocomposite. The broad peak in the $15-30°$ range in sample S2 indicates the coexistence of the organic component, whereas in S3, this broad peak becomes less prominent due to the dominant diffraction signals of the ZnO crystalline phase.The crystallite sizes of the ZnO phase were calculated using the Debye–Scherrer equation [38], resulting in values of 30.4 nm and 31.2 nm for samples S2 and S3, respectively. These values are nearly identical, confirming the consistent crystal size of ZnO nanoparticles across different concentrations.

XRD analysis revealed that the sample without ZnO exhibits an amorphous nature, whereas the incorporation of ZnO nanoparticles results in the formation of a hexagonal crystalline structure. Increased peak intensities in the higher ZnO content sample indicate enhanced crystallinity. ZnO

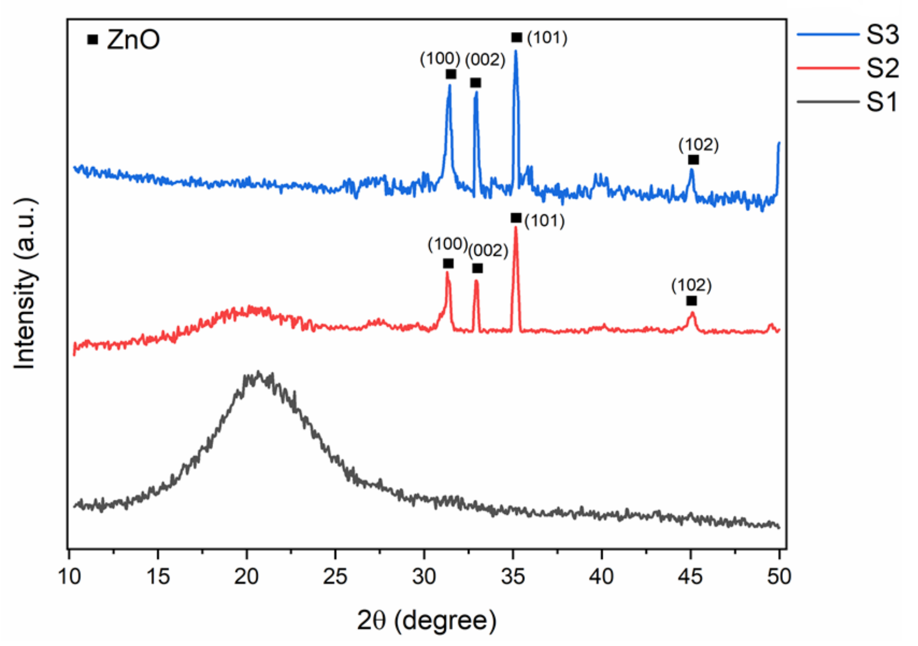

Figure 1. XRD diffraction patterns of samples without nanoparticles (S1) and those containing 5 wt.% (S2) and 10 wt.% (S3) ZnO nanoparticles.

crystallite sizes ranged from 30 to 31 nm, and the presence of the organic component in the nanocomposites was confirmed.

3.2 FT-IR analysis

In figure 2, the FT-IR spectra of the nanocomposites containing different concentrations of zinc oxide NPs are presented. From the FT-IR spectra, the absorption band observed at 3332 cm^{-1} corresponds to the stretching vibrations of O–H and N–H bonds in the polyurethane structure and other composite components [39]. The peaks located at 2933 cm^{-1} and 2857 cm^{-1} are attributed to the stretching vibrations of C–H bonds in aliphatic structures such as polyglycerol and itaconic acid [40]. In addition, the absorption peak at 1730 cm^{-1} represents the stretching vibration of the C=O bond in the acidic structure of itaconic acid [41]. After incorporating ZnO nanoparticles into the composite, the intensity of these characteristic peaks markedly decreased, and the C=O stretching band shifted to approximately 1683 cm^{-1}. This shift indicates that the carboxylic functional groups in the composite matrix act as effective binding sites for ZnO nanoparticles and that the presence of ZnO alters the

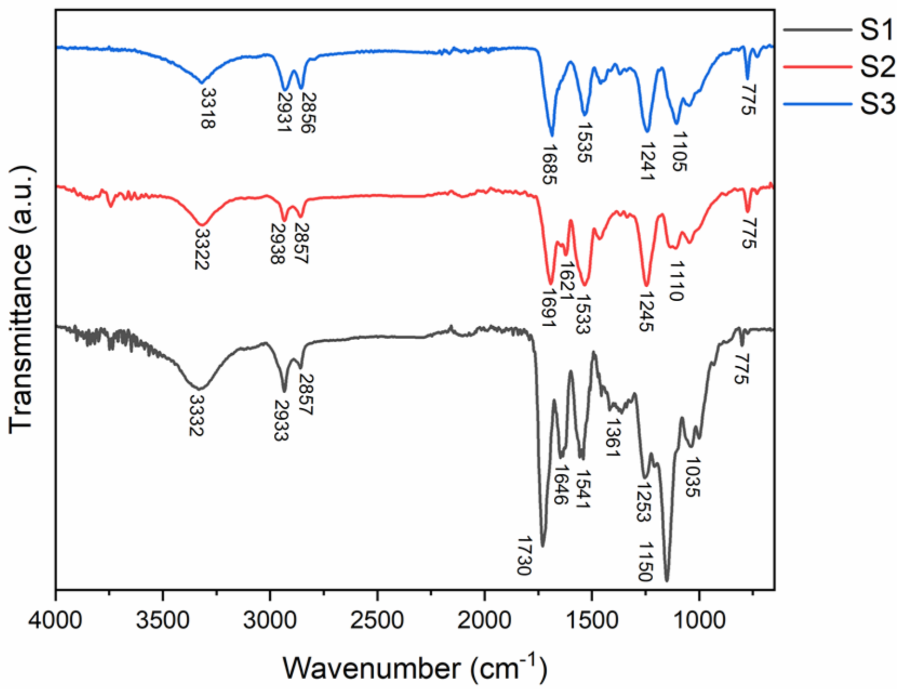

Figure 2. FT-IR spectra of porous scaffolds without nanoparticles (S1) and those containing 5 wt.% (S2) and 10 wt.% (S3) ZnO nanoparticles.

vibrational behavior of these functional groups.

The peaks appearing at 1646 cm^{-1} and 1541 cm^{-1} correspond to the bending vibrations of O–H, the stretching of C=O in polyurethane, and the bending vibrations of N–H in amine-containing structures [42]. The reduction in intensity and slight shift of these peaks toward lower wavenumbers suggest that less energy is required for bond vibrations when ZnO nanoparticles are present. Furthermore, increasing the nanoparticle concentration led to a further decline in peak intensities, providing clear evidence of strong interactions between ZnO and the organic matrix.

The peaks detected at 1361 cm^{-1} and 1253 cm^{-1} are associated with C–H bending and C–N stretching vibrations, respectively, in the organic components of the nanocomposites [43]. Similarly, the bands at 1150 cm^{-1} and 1035 cm^{-1} correspond to the stretching vibrations of C–OH and C–O–C bonds in itaconic acid, polyglycerol, and polyurethane [44]. The decreased intensity of these peaks in the presence of ZnO nanoparticles further confirms the interaction between the nanoparticles and the organic bonds, verifying the successful synthesis of ZnO-containing nanocomposites.

Characteristic asymmetric and symmetric stretching vibrations of Zn–O bonds were observed at 775 cm^{-1} and 728 cm^{-1}, respectively [45]. An increase in ZnO content from 5 to 10 wt.% resulted in enhanced Zn–O peak intensities, confirming the higher nanoparticle loading in the synthesized nanocomposites.

Overall, the FT-IR results demonstrate that ZnO nanoparticles form direct interactions with the functional groups of the organic matrix. The reduction in peak intensities and shifts toward lower wavenumbers confirm the formation of Zn–O bonds and indicate the mechanical stabilization of the nanoparticles within the composite. Moreover, increasing ZnO concentration strengthens these interfacial interactions, which may facilitate controlled Zn^{2+} release, thereby enhancing both the antibacterial activity and biocompatibility of the scaffolds.

3.3 SEM analysis

The results of the SEM analysis for the samples containing 0, 5, and 10 wt.% zinc oxide nanoparticles are shown in figure 3.

According to figure 3(a), the polymer sample without zinc oxide (ZnO) nanoparticles exhibits noticeable cavities and surface defects. These cavities are intrinsic to the polymer matrix and may also result from the salt-leaching process used during scaffold fabrication. Similar surface features have been reported in previous studies on comparable polymer composites [46].

In figure 3(b) for the S1 sample, both large cavities and smaller pores are visible. Image analysis using ImageJ software showed that the large cavities observed in figure 3(a) range from approximately 30 to 360 μm, with an average diameter of 132 μm and a standard deviation of 92 μm. The smaller pores have an average size of 1.5 μm and a standard deviation of 1.1 μm, indicating a bimodal pore structure.

As shown in figure 3(c), for the scaffold containing 5 wt.% ZnO nanoparticles (S2), the diameter of the large cavities slightly decreased, with an average of 112 μm and a standard deviation of 58 μm. In figure 3(d), the fine microscale porosity is no longer visible, suggesting that the ZnO nanoparticles filled the smaller voids and contributed to the reduction in overall cavity size.

For the sample containing 10 wt.% ZnO nanoparticles (S3), figure 3(e) reveals large cavities with an average diameter of approximately 92 μm and a standard deviation of 36 μm, indicating a further reduction in pore size. However, figure 3(f) shows the formation of aggregated clusters of ZnO nanoparticles, with an average cluster size of 1.9 μm and a standard deviation of 0.7 μm, suggesting that excess nanoparticles tended to accumulate within the nanocomposite microstructure.

Overall, these observations demonstrate that the optimal ZnO concentration is 5 wt.%, as higher concentrations promote nanoparticle agglomeration and the formation of clustered regions, which may adversely affect pore uniformity and scaffold performance.

3.4 EDS and elemental mapping analysis

The results of elemental analyses are shown in figure 4 and figure 5, respectively, for the prepared nanocomposites containing 5 and 10 wt.% zinc oxide NPs.

According to the EDS results presented in figure 4, the elemental composition of the nanocomposite confirms the presence of zinc (3.65%) and oxygen (29.52%), originating from the incorporated ZnO nanoparticles. In addition, carbon (60.87%) and nitrogen (5.96%) were detected, corresponding to the polymeric matrix of the composite. Elemental mapping further reveals that, although ZnO nanoparticles form small localized clusters in certain regions of the microstructure (indicated by red arrows), their overall dispersion within the matrix is generally uniform and satisfactory.

As shown in figure 5, the sample containing 10 wt.% ZnO nanoparticles exhibited higher elemental weight percentages of zinc (7.09%) and oxygen (30.24%) compared to the 5 wt.% ZnO sample (S2). Conversely, the relative mass percentages of carbon (58.76%) and nitrogen (3.91%), which represent the polymeric phase, were slightly lower. Elemental mapping in figure 5(b) clearly demonstrates zinc enrichment in specific localized areas, while other regions show no detectable zinc signal, indicating non-uniform nanoparticle distribution and severe agglomeration in the S3 sample.

Overall, EDS and elemental mapping analyses confirm that at 5 wt.% ZnO, nanoparticles are well-dispersed throughout the polymeric matrix, maintaining compositional homogeneity. However, at 10 wt.% ZnO, pronounced aggregation and clustering occur, resulting in reduced elemental uniformity and potential deterioration of the composite's mechanical and biological performance.

3.5 Contact angle results

In figure 6, the contact angle values for the prepared nanocomposites are displayed as bar diagrams.

According to the results presented in figure 6, the polyurethane–polyglycerol–itaconic acid scaffold without ZnO nanoparticles (S1) exhibited a significantly lower contact angle than the other samples, indicating a highly hydrophilic surface. This pronounced hydrophilicity is at-

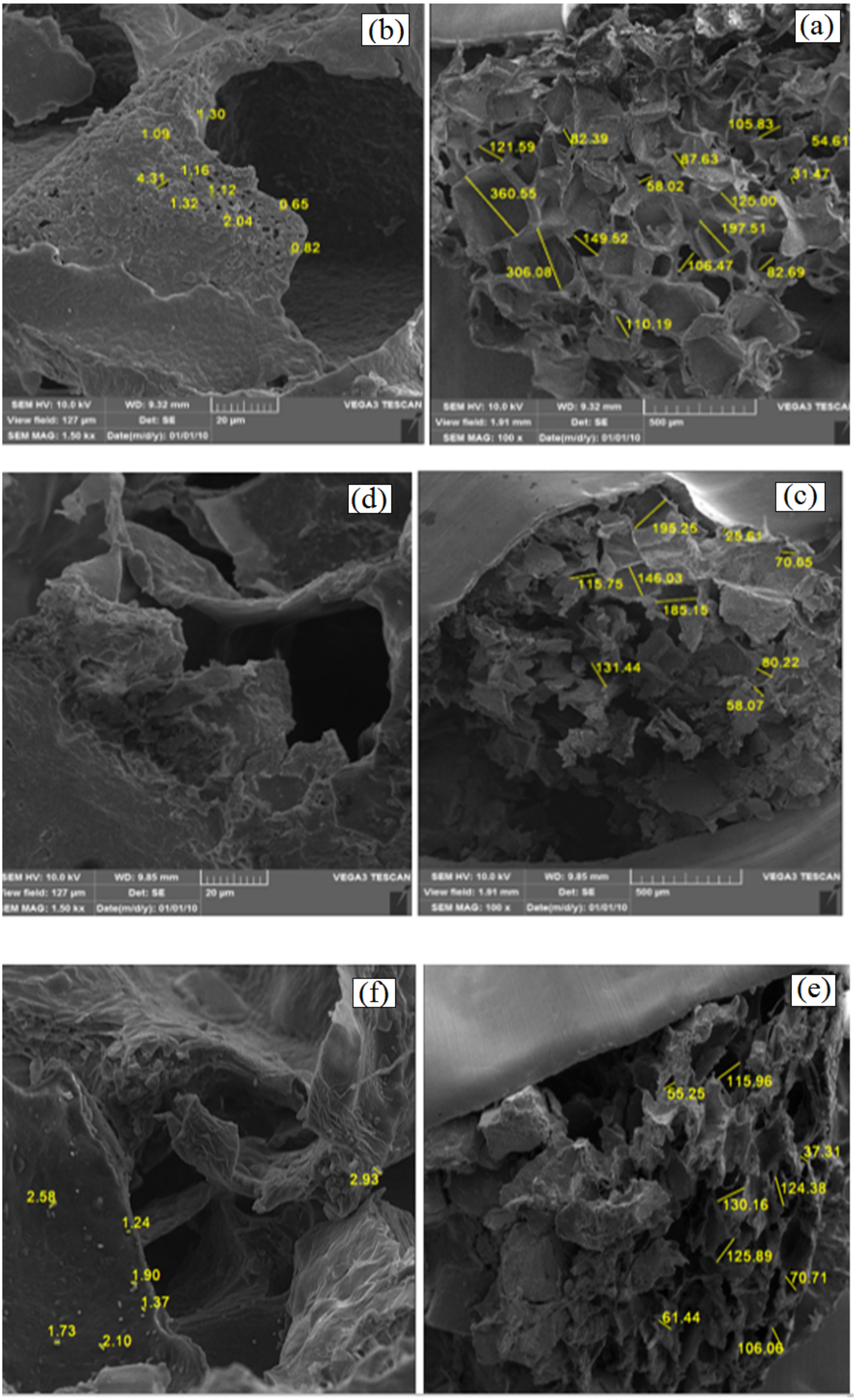

Figure 3. SEM images of scaffolds without nanoparticles (S1), with 5 wt.% ZnO (S2), and 10 wt.% ZnO (S3) at 100× and 1500× magnifications.

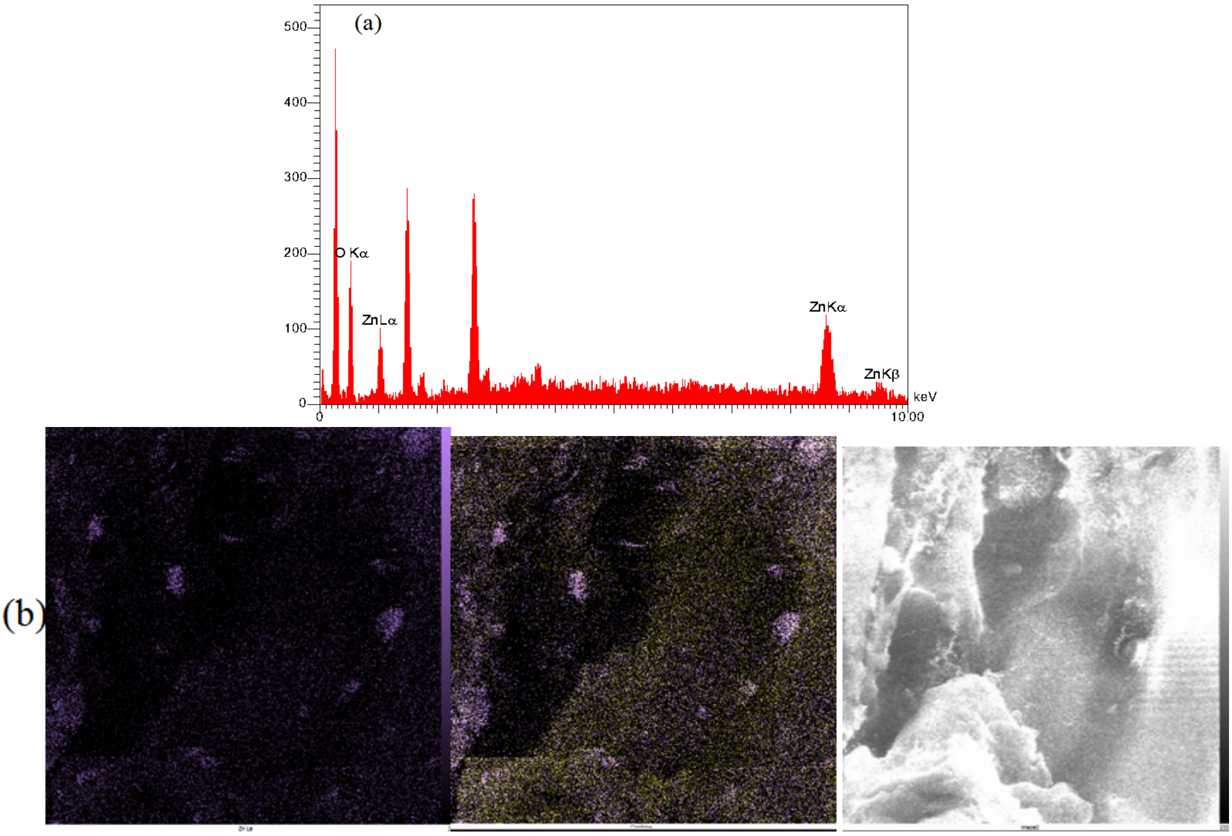

Figure 4. EDS spectrum (a) and elemental mapping of the S2 sample (5 wt.% ZnO) (b).

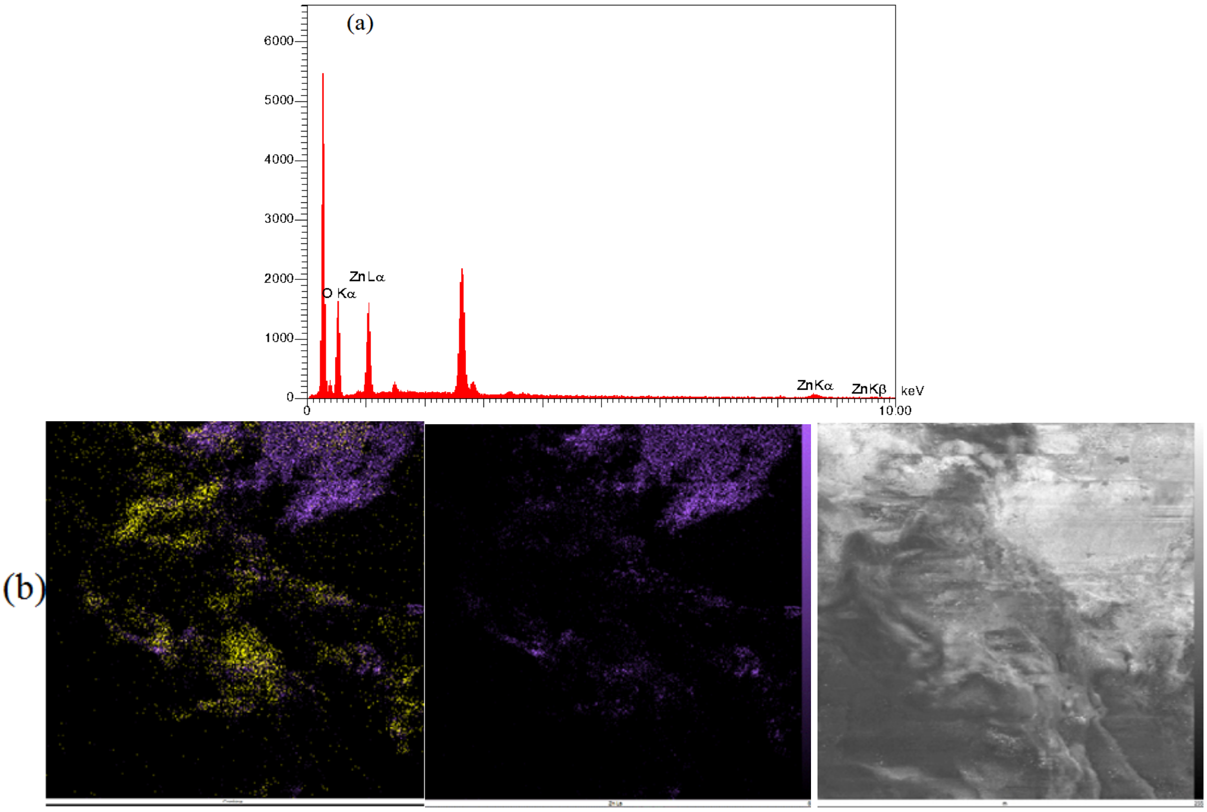

Figure 5. EDS spectrum (a) and elemental mapping of the S3 sample (10 wt.% ZnO) (b).

tributed to the abundance of hydroxyl and carboxylic functional groups in the composite structure, as confirmed by the FT-IR analysis. Water molecules readily form hydrogen bonds with these polar groups, enabling rapid spreading of the water droplet over the surface. Comparable hydrophilic behavior has been reported for similar polymeric composites in previous studies [47].

Upon incorporation of ZnO nanoparticles, the surface hydrophobicity of the composites increased markedly. For samples containing 5 wt.% and 10 wt.% ZnO nanoparticles, the contact angle increased by approximately 10-fold and 12-fold, respectively, compared with the nanoparticle-free sample (S1). This increase can be attributed to the enhanced surface roughness caused by the presence of ZnO nanoparticles and the entrapment of microscopic air pockets beneath the water droplet, which reduce the effective solid–liquid contact area. A similar trend was observed by khan et al. when incorporating ZnO nanoparticles into polyvinyl alcohol (PVA) nanocomposites [48].

3.6 Equilibrium water absorption (EWA) analysis

To evaluate the equilibrium water absorption behavior of the prepared nanocomposites, the samples were weighed at specific time intervals of 0, 1, 2, 3, 4, 18, and 24 hours. The variations in absorbed water weight and swelling percentage are presented in figure 7.

Samples S1 and S2 exhibited a rapid increase in water absorption during the initial hours, followed by a gradual stabilization, whereas S3 showed minimal weight change throughout the test. After 18 hours of immersion, water uptake reached equilibrium for all samples. The corresponding equilibrium water absorption values were 442.15% for S1, 470% for S2, and 22.52% for S3.

The observed behavior can be explained by differences in the density and porosity of the nanocomposites. Samples S1 and S2 possessed lower densities, allowing greater water penetration into the porous network. Incorporation of 5 wt.% ZnO nanoparticles (S2) had a negligible impact on water absorption, indicating that the moderate addition of nanoparticles did not hinder the hydrophilic nature of the matrix. However, increasing the ZnO content to 10 wt.% (S3) caused a significant reduction in water uptake, as the nanoparticles filled the microvoids within the polymer matrix, resulting in a denser and less permeable structure.

Overall, the water absorption analysis confirms that scaffolds without ZnO or with 5 wt.% ZnO exhibit high hydrophilicity and swelling capacity, which are favorable for cell infiltration and nutrient diffusion. In contrast, the 10 wt.% ZnO scaffold demonstrates limited water uptake, consistent with the increased compactness of the nanocomposite structure.

3.7 Biodegradability test

Based on the water absorption curves (figure 8(a)), the sample weights measured after 18 hours of immersion were used as reference points for calculating the degree of degradation. Due to the irregular fluctuations observed in sample weights (figure 8(b)) and the water absorption behavior of the synthesized scaffolds, it appears that weight loss from polymer degradation was partially offset by simultaneous water uptake. Therefore, to more accurately assess degradation, the final dry weight after 14 days of immersion was compared with the initial dry weight of each sample.

Based on the water absorption curves (figure 8(a)), the sample weights measured after 18 hours of immersion were used as reference points for calculating the degree of degradation. Due to the irregular fluctuations observed in sample weights (figure 8(b)) and the water absorption behavior of the synthesized scaffolds, it appears that weight loss from polymer degradation was partially offset by simultaneous water uptake. Therefore, to more accurately assess degradation, the final dry weight after 14 days of immersion was compared with the initial dry weight of each sample.

According to figure 8(b), sample S1 displayed an overall decreasing trend, although slight increases in weight were recorded during intermediate measurements. After 7 days, noticeable degradation occurred, but water absorption compensated for part of the weight loss. Comparing the final and initial dry weights, S1 exhibited a total degradation of 99.19% after 14 days of immersion.

In contrast, sample S2 showed minor degradation after the first day, followed by a temporary reduction in degradation rate due to increased water absorption. After 7 days, the degradation rate surpassed the absorption rate, leading to a net weight decrease. Similar fluctuations were observed by day 14, with a slight increase in weight toward the end of the test. Overall, S2 experienced 25.10% degradation over the 14-day period, displaying a similar pattern to S1

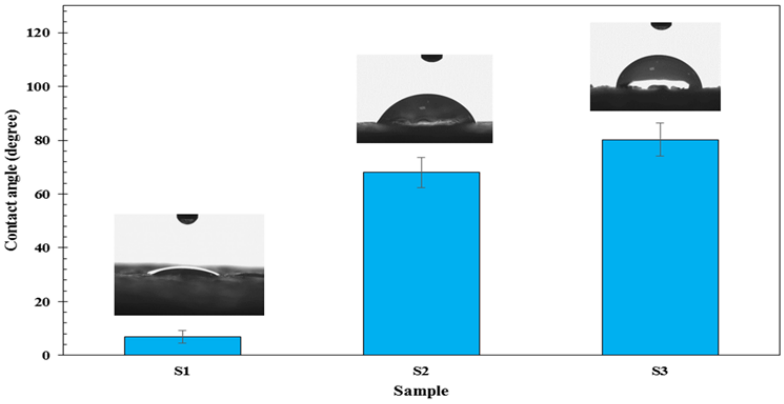

Figure 6. Bar charts showing the contact angle values of the prepared nanocomposites.

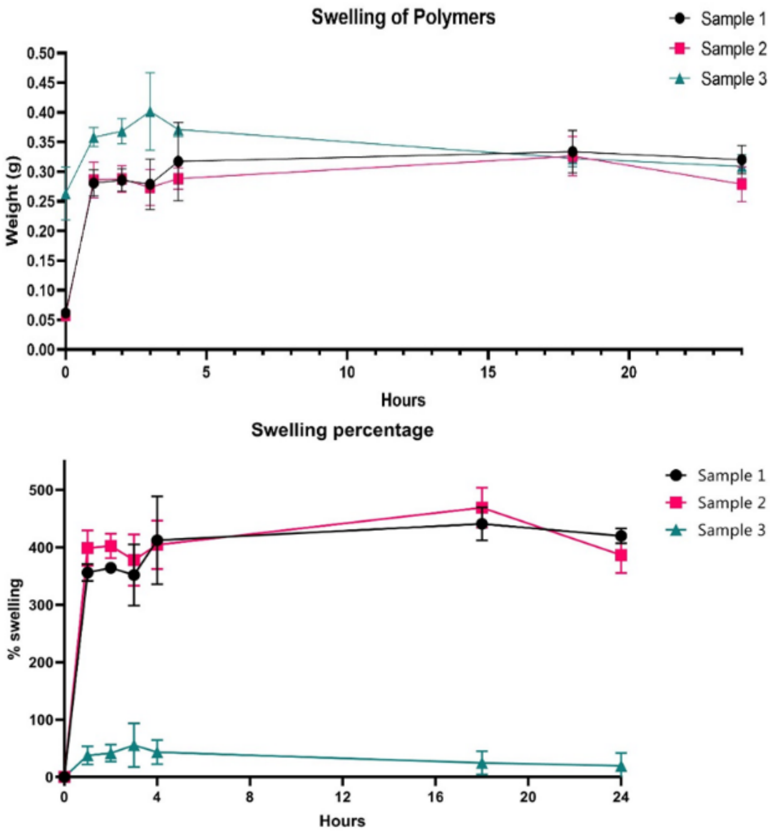

Figure 7. Equilibrium water absorption over 24 hours: (a) weight increase and (b) swelling percentage.

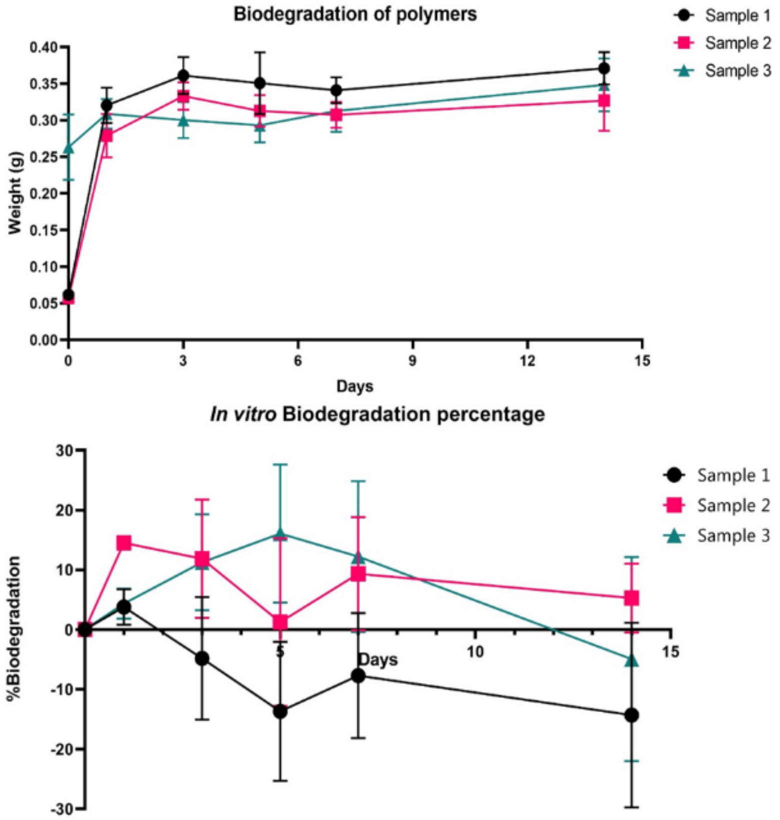

Figure 8. (a) Weight changes and (b) biodegradation variations of the samples over 14 days.

but with a lower total degradation degree.

Sample S3 initially exhibited an increasing trend in degradation during the first five days of immersion, followed by a reduction in weight loss rate and a gradual increase in sample weight from day 5 to day 14. Compared with its initial dry weight, S3 exhibited 30.58% total degradation after 14 days. The relatively higher density of S3, compared to S1 and S2, allowed for moderate degradation while still enabling partial water penetration, resulting in the observed late-stage weight gain.

Overall, these findings indicate that ZnO concentration significantly influences scaffold degradation behavior. The 5 wt.% ZnO scaffold (S2) achieved the most stable degradation profile, suggesting a controlled balance between structural integrity and biodegradability, which is desirable for guided bone regeneration applications.

The degradation analysis indicated that S1 (without ZnO) experienced the highest overall degradation (99.19%), whereas S2 and S3 (with 5 and 10 wt.% ZnO) showed significantly lower degradation (25.10% and 30.58%, respectively). Incorporation of ZnO nanoparticles increased scaffold density, reduced degradation rate, and caused weight fluctuations due to water absorption during the 14-day period.

3.8 Antibacterial activity results

To evaluate the antibacterial properties of the samples, turbidity measurements were performed at 600 nm. Since the observed turbidity does not exclusively indicate the presence of live bacteria and can be affected by factors such as extract turbidity or dead bacteria, resazurin dye was employed for accurate quantification of viable bacteria. Given the acceptable agreement between the turbidity test results (figure 9) and the resazurin emission method (figure 10), the latter was used for further investigations.

The antibacterial assay plates following incubation with resazurin dye are presented in Figure S1 (Supplementary Document). As illustrated in figure 10, which shows turbidity measurements at 600 nm, the S1 sample (without ZnO nanoparticles) exhibited no bactericidal or inhibitory effects against either *Escherichia coli* or *Staphylococcus aureus*. In contrast, sample S2 (100 µL) demonstrated strong inhibitory activity against *E. coli*. This behavior can be attributed to the lower degradation rate of the scaffold, resulting in a gradual and controlled release of ZnO nanoparticles, the active antibacterial component. For sample S3, the nanocomposite displayed notable inhibitory effects against *Staphylococcus aureus* at concentrations of 100, 50, and 25 µL. This enhanced antibacterial performance is likely due to the higher degradation rate of S3 compared to the other scaffolds, which promoted a greater release of ZnO

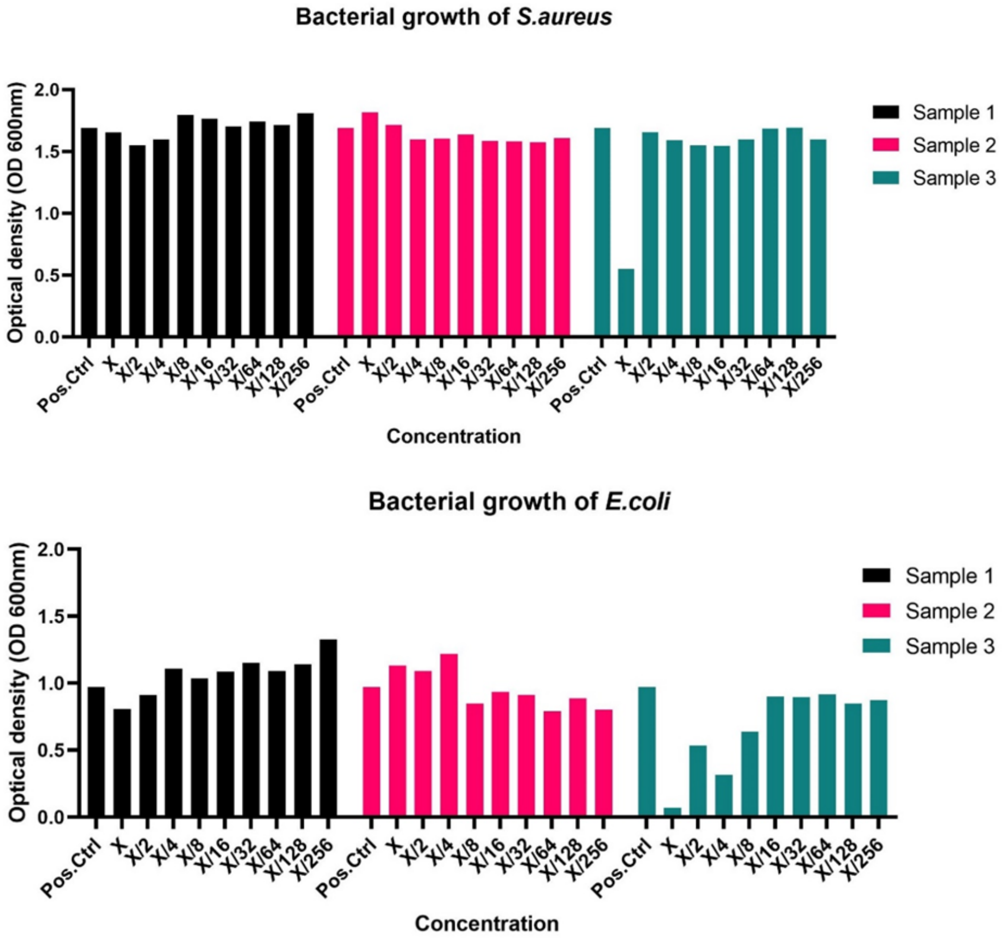

Figure 9. Bar charts showing bacterial absorbance at 600 nm for (a) *S. aureus* and (b) *E. coli* in the presence of polymer extracts.

nanoparticles into the surrounding medium. The increased availability of ZnO thereby intensified antibacterial activity. Although the precise mechanisms of ZnO-mediated antibacterial action remain under investigation, several hypotheses have been proposed. These include electrostatic interactions between ZnO nanoparticles and bacterial cell membranes, as well as the generation of reactive oxygen species (ROS) within bacterial structures, which can damage cellular components and inhibit bacterial proliferation.

3.9 Cell adhesion results

To evaluate the cell adhesion properties of the prepared nanocomposites, scanning electron microscopy (SEM) was performed, and the obtained micrographs are shown in figure 11. According to figure 11(a–b), the S1 sample exhibits a highly porous structure, and several pores contain adhered and stabilized cells, confirming the scaffold's basic biocompatibility. As shown in figure 11(c–d), a notable reduction in surface porosity is observed for the S2 sample compared to S1. In addition, a greater number of adhered cells are evident on the polymeric surface of S2, indicating that the presence of ZnO nanoparticles at an optimal concentration (5 wt.%) enhances cell attachment and proliferation. Many of the small white spots observed in these micrographs correspond to ZnO nanoparticles, which appear smaller than the attached cells. The SEM micrographs of sample S3 are presented in figure 11(e–f). Compared with S1, S3 shows a denser microstructure with lower porosity, consistent with nanoparticle filling and aggregation effects. However, the surface morphology of S3 appears less uniform than that of S2, and no improvement in cell adhesion was observed when the ZnO nanoparticle concentration was increased to 10 wt.%.

Overall, surface porosity and ZnO nanoparticle distribution play crucial roles in cell attachment. The S2 scaffold exhibited the most favorable cell adhesion behavior, attributed to the uniform dispersion of ZnO nanoparticles and well-preserved porosity, while S3 showed reduced surface uniformity and impaired cellular attachment due to nanoparticle aggregation.

3.10 MTT cell viability results

The cell viability results at 24 and 48 hours are presented in figure 12. According to the data, Sample S1 did not exhibit any significant difference compared to the control at either time point, indicating acceptable baseline biocompatibility. In contrast, Sample S2 showed a significant increase in cell proliferation (approximately 10% higher than the control) after 24 hours; however, no notable difference was observed at 48 hours, suggesting that S2 promotes early-stage cell growth without inducing cytotoxicity over time.

Sample S3 displayed marked cytotoxicity at both 24 and

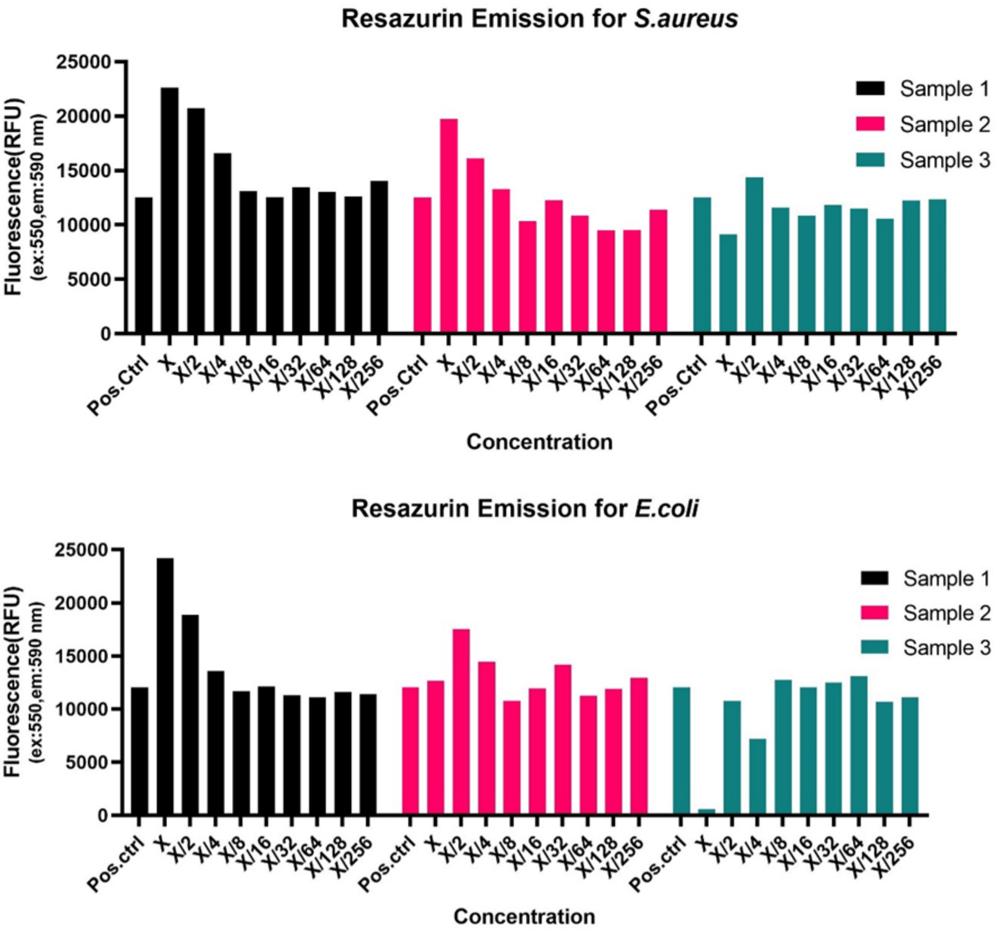

Figure 10. Resazurin fluorescence measurements for (a) *S. aureus* and (b) *E. coli*.

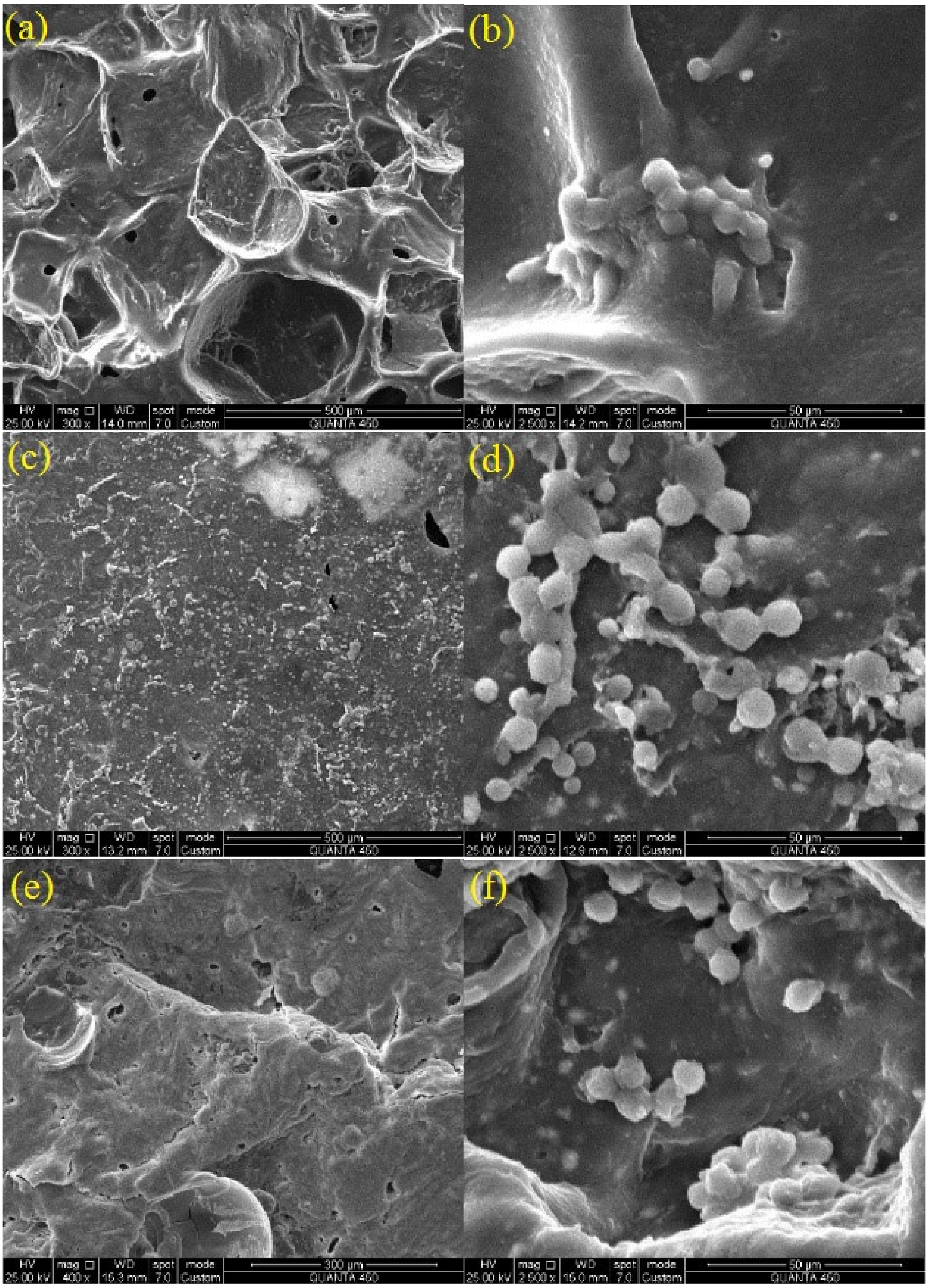

Figure 11. SEM micrographs of (a and b) S1, (c and d) S2, and (e and f) S3 at two different magnifications.

48 hours. Wells containing 2.5 µL of extract showed an average viability of 75% at 24 hours and 50% at 48 hours, whereas other wells exhibited less than 15% viability. These observations are consistent with the degradation data, as the lower degradation rates of S1 and S2 produced extracts with lower ZnO nanoparticle concentrations, resulting in reduced cytotoxicity. By contrast, the higher ZnO content and faster degradation rate of S3 contributed to increased extract toxicity, impairing cell survival.

Overall, these results confirm that ZnO concentration and scaffold degradation rate are critical factors in determining cell viability. Samples with lower ZnO content (S1 and S2) maintained acceptable biocompatibility, while excessive nanoparticle loading (S3) caused severe cytotoxic effects. This underscores the importance of optimizing nanoparticle concentration to balance antibacterial activity with cellular safety in biomedical scaffold applications.

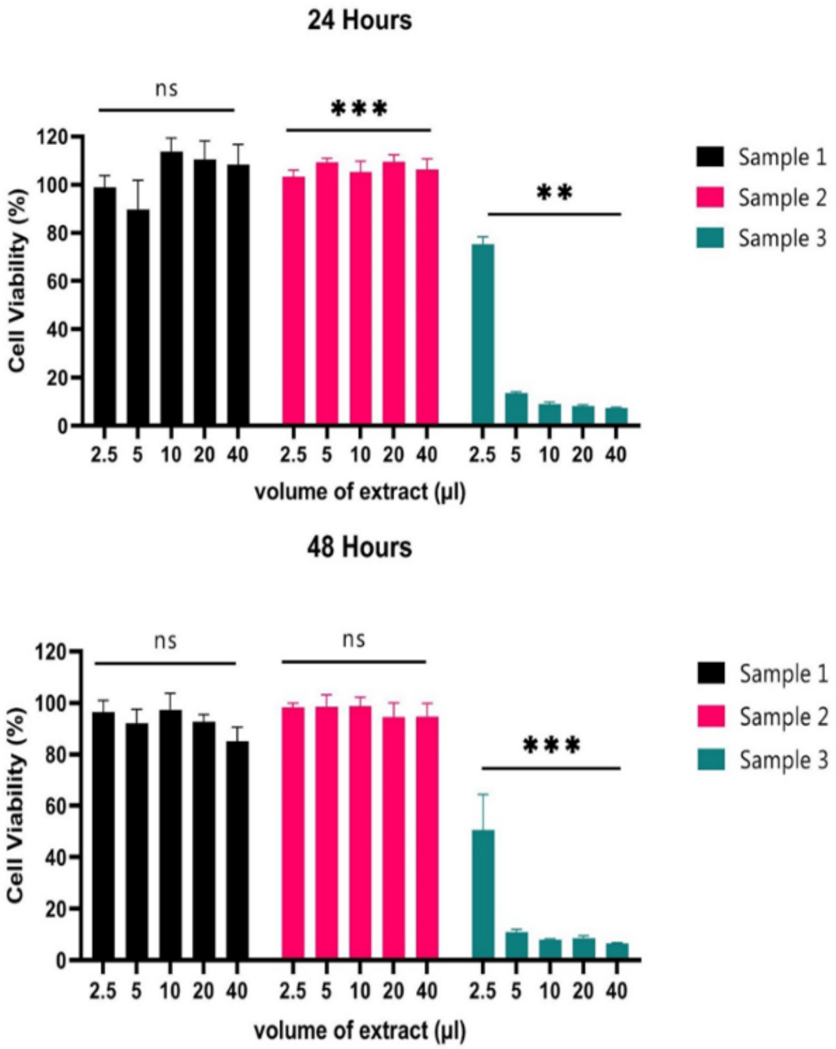

Figure 12. Cell viability at (a) 24 hours and (b) 48 hours.

3.11 Microstructural, physical, and chemical characterization of PU/PGIt-ZnO scaffolds

The microstructural, physical, and chemical properties of PU/PGIt-ZnO scaffolds were characterized, and the results are presented in figures 12 and 13.

SEM and EDS analyses revealed that in the 5 wt.% ZnO sample (S2), nanoparticles were uniformly dispersed within the polymer matrix, resulting in a porous structure conducive to cell proliferation and biocompatibility. In contrast, the 10 wt.% ZnO sample (S3) exhibited nanoparticle aggregation and clustering, which reduced structural homogeneity and compromised biocompatibility.

XRD analysis confirmed the presence of characteristic ZnO diffraction peaks, demonstrating its role in stabilizing the crystalline phase of the scaffold. Complementary FTIR spectra showed interactions between ZnO nanoparticles and the hydroxyl and carboxylic groups of the polymer matrix, which contributed to enhanced mechanical properties and structural stability.

Surface characterization further indicated that S2 exhibited favorable hydrophilicity, promoting effective cell–scaffold interactions, whereas S1 showed lower surface hydrophilicity, and S3 displayed unfavorable surface alterations caused by nanoparticle agglomeration.

3.12 *In vitro* evaluation results

The *in vitro* performance of the PU/PGIt-ZnO scaffolds was assessed, and the results are presented in figures 14 and 15. The degradation test in aqueous medium demonstrated that the S2 scaffold (5 wt.% ZnO) exhibited a controlled degradation rate, suitable for bone tissue regeneration. Cytotoxicity assessment using L929 fibroblast cells showed that S2 achieved the highest cell viability and proliferation, whereas S3 (10 wt.% ZnO) induced significant cytotoxic effects, identifying 5 wt.% ZnO as the optimal concentration for maintaining biocompatibility.

Regarding antibacterial activity, S2 effectively inhibited bacterial growth while maintaining a balance between antimicrobial properties and cytocompatibility. In comparison, the ZnO-free scaffold (S1) showed weaker antibacterial performance, and although S3 exhibited enhanced antibacterial effects, its clinical applicability was limited due to cytotoxicity.

Statistical analysis (P-values) confirmed significant differences among the groups, further highlighting the superiority of the 5 wt.% ZnO scaffold in terms of overall performance,

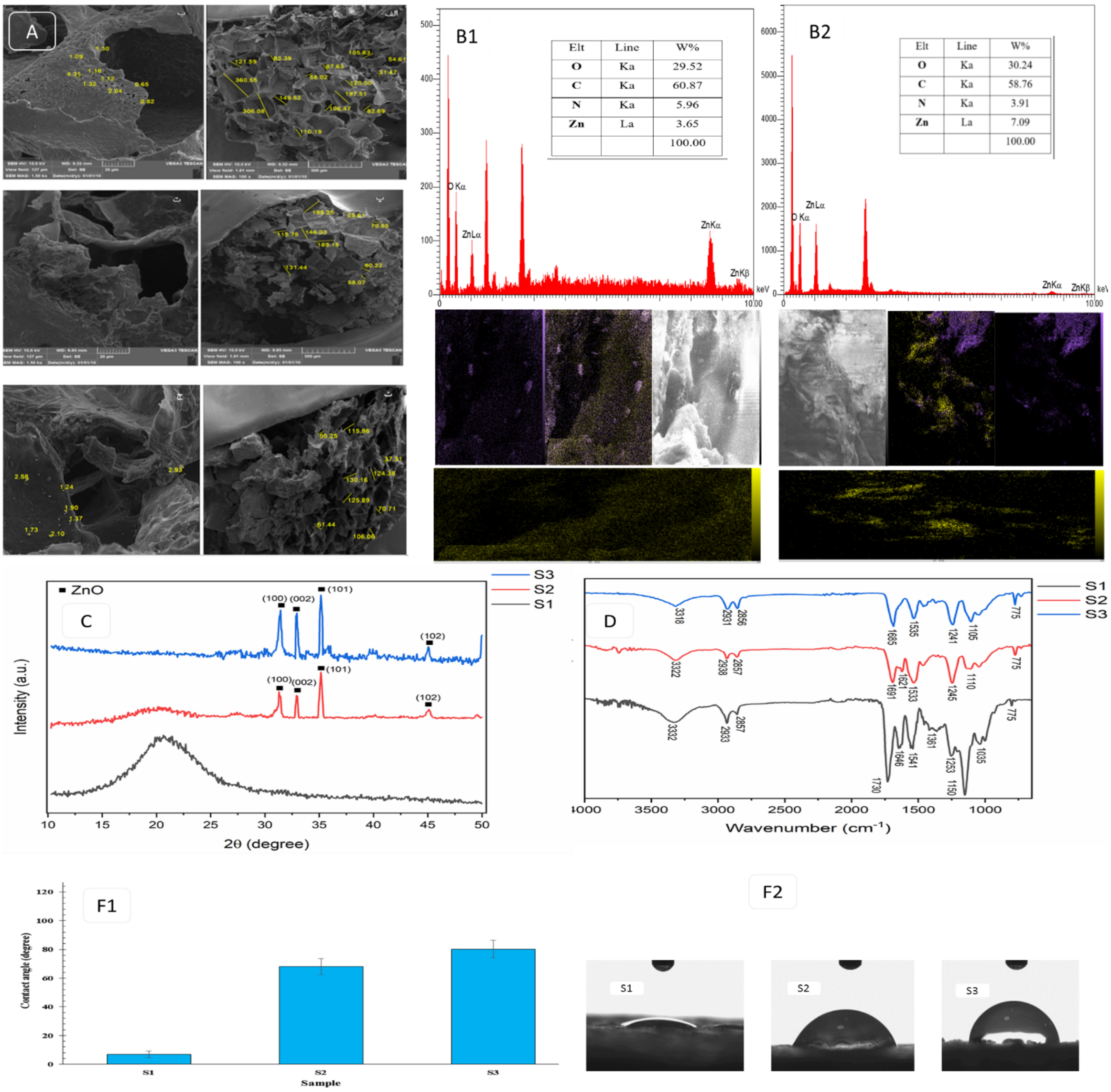

Figure 13. SEM micrograph(A); EDS spectrum of ZnO in sample S2(B1); EDS spectrum of ZnO in sample S3(B2). XRD pattern(C); FTIR spectrum(D); contact angle plot(F1); water droplet images of the three samples(F2).

including degradation behavior, cytocompatibility, and antibacterial efficacy.

4. Conclusion

In this study, polyurethane–poly(glycerol itaconate) scaffolds reinforced with zinc oxide (ZnO) nanoparticles at 0%, 5%, and 10% w/w were designed and evaluated to investigate the effects of ZnO concentration on microstructure, surface properties, biocompatibility, cell adhesion, water uptake, degradation, cytotoxicity, and antibacterial activity within the context of guided bone regeneration (GBR).

Morphological and structural analyses revealed that in the scaffold containing 5% ZnO (S2), nanoparticles were uniformly dispersed throughout the polymer matrix, creating a porous structure conducive to cell proliferation. In contrast, the 10% ZnO scaffold (S3) exhibited nanoparticle clustering and aggregation, which could compromise biocompatibility and result in uneven cell distribution. Recent studies have shown that ZnO nanoparticles at optimal concentrations ($3-5\%$ w/w) not only enhance surface hydrophilicity and cell adhesion, but also stimulate osteoblast differentiation through the gradual release of Zn^{2+} ions, leading to increased expression of bone-related genes, such as ALP and Runx2 [49, 50].

XRD analysis confirmed that ZnO incorporation stabilized the crystalline phase of the scaffolds, with characteristic diffraction peaks corresponding to the (100), (002), (101), and (102) planes. FTIR spectra demonstrated interactions between ZnO nanoparticles and matrix functional groups, including hydroxyl and carboxyl groups, which contributed to enhanced mechanical properties and structural stability. Polyurethane, as a highly elastic polymer, plays a key role in evenly distributing mechanical stresses and enhancing the tensile strength of the scaffold. Its highly flexible soft chains reduce brittleness and impart pseudo-elastomeric behavior, which is essential for bone tissue applications [20] [51].

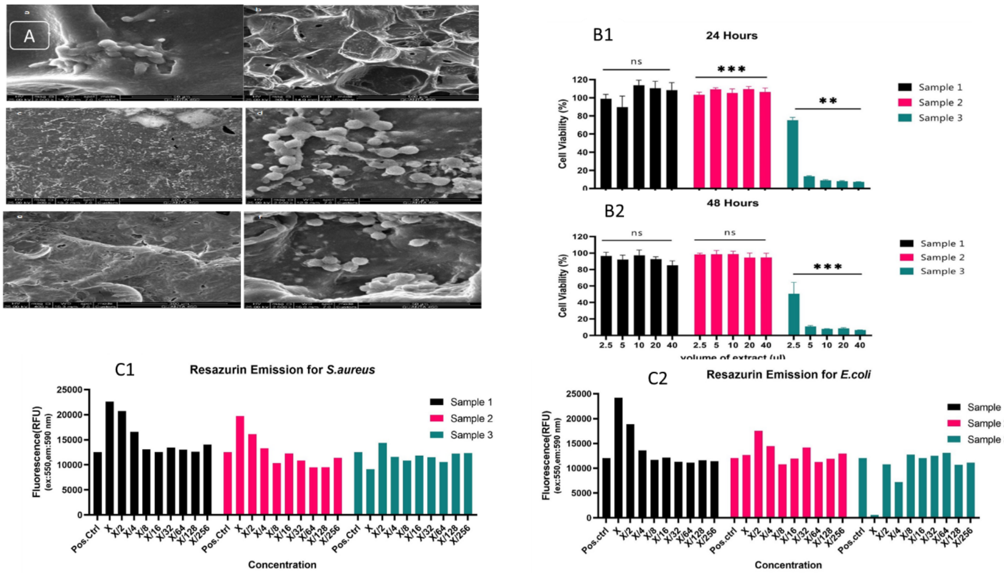

Figure 14. Cell adhesion(A); antibacterial activity(B1–B2); cytotoxicity assay(D1–D2).

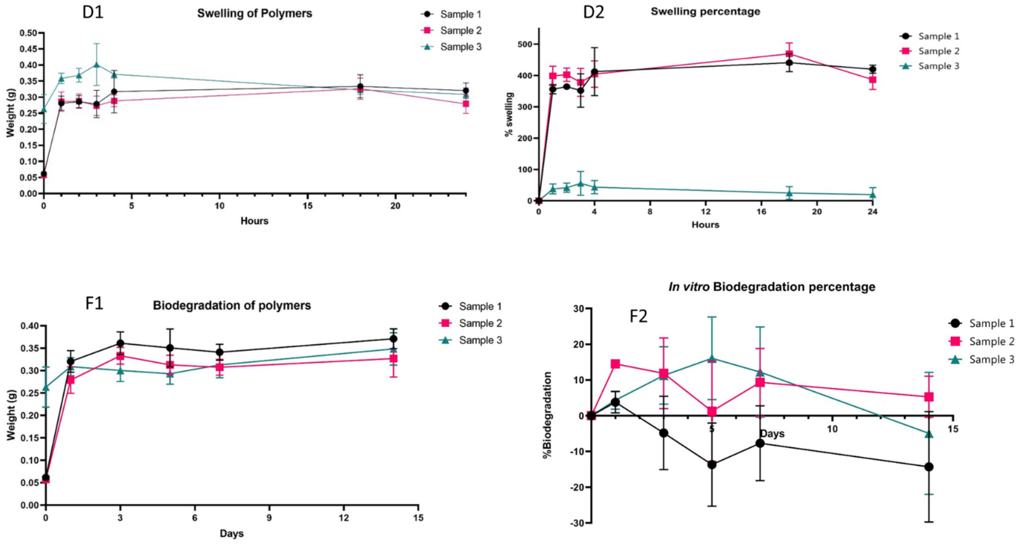

Figure 15. Water uptake(D1–D2); degradation rate(F1–F2).

Surface characterization showed that S2 possessed a hydrophilic surface favorable for cell–scaffold interactions, as indicated by contact angle and equilibrium water absorption measurements. The ZnO-free scaffold (S1) exhibited lower hydrophilicity, while S3 displayed undesirable surface changes due to nanoparticle aggregation. Degradation studies indicated that S2 degraded at a controlled rate compatible with bone tissue regeneration, highlighting its clinical relevance, as gradual scaffold degradation is essential to match new tissue formation.

Polyglycero itaconate, due to the presence of active carboxyl and hydroxyl groups, exhibits a high capacity for forming hydrogen bonds with cells, thereby improving bioadhesion and enabling gradual scaffold degradation. Moreover, the presence of itaconate units in the polymer backbone provides sites for covalent bonding with nanoparticles, enhancing the chemical stability of the scaffold [22, 52].

Biological evaluations using L929 fibroblast cells demonstrated that S2 supported the highest cell viability and proliferation, with cells adhering well to the scaffold surface. In contrast, S3 (10% ZnO) induced significant cytotoxicity, indicating that excessive ZnO disrupts biological balance. These findings suggest that 5% ZnO represents the optimal concentration for functional scaffolds.

Antibacterial assessments showed that S2 effectively inhibited bacterial growth while maintaining biocompatibility. S1 exhibited weak antibacterial activity, and although S3 displayed stronger antibacterial effects, its cytotoxicity limits potential clinical application. Statistical analyses confirmed significant differences between groups, further supporting 5% ZnO as the optimal functional concentration for balancing mechanical, biological, and antibacterial performance in GBR scaffolds.

Key features of an effective scaffold for bone regeneration include optimal porosity ($50-70\%$), high biocompatibility, controlled water uptake, and bioactive release capability. The present scaffold, with its porous network and the simultaneous combination of a soft phase (polyurethane) and a bioactive phase (ZnO and polyglycero itaconate), provides an ideal environment for cell infiltration and new bone matrix formation [26].

In summary:

S1 (0% ZnO) exhibited acceptable biocompatibility but demonstrated insufficient antibacterial activity.

S2 (5% ZnO) achieved the best balance among biocompatibility, surface hydrophilicity, controlled degradation rate, cell adhesion, and antibacterial activity.

S3 (10% ZnO) showed high cytotoxicity and nanoparticle aggregation, which limited its applicability.

This study was limited to *in vitro* analyses, including SEM/EDS-MAP, XRD, FTIR, contact angle and water absorption tests, degradation, cytotoxicity, and antibacterial evaluations. For conclusive validation, *in vivo* studies are recommended to assess immune response, bone regeneration rate, and mechanical durability under physiological conditions.

Based on findings from similar *in vivo* studies, such scaffolds can be applied for the regeneration of jaw, cranial, and long bone defects and may even serve as delivery platforms for growth factors, such as BMP-2 or VEGF. The combination of high biocompatibility, adequate mechanical strength, and antibacterial activity makes this system a promising candidate for applications in orthopedics and dental implants [17].

Overall, the polyurethane–poly(glycerol itaconate) scaffold containing 5% ZnO exhibited superior performance in guided bone regeneration (GBR) compared to conventional polymer scaffolds. While collagen membranes are biocompatible and widely used, they degrade rapidly and have limited mechanical strength [53]. Synthetic polymers such as PLA and PGA provide greater stability, but often lack optimal porosity and bioactive factor release [27].

In comparison, the proposed scaffold combines uniform porosity, biocompatibility, controlled ZnO distribution, effective antibacterial activity, and balanced degradability [29]. With its combination of biocompatibility, mechanical properties, and antibacterial effects, this scaffold represents a promising platform for bone regeneration and potential applications in orthopedics and dentistry.

Authors contributions

All authors contributed equally to the conception, design, execution, and writing of this work. All authors read and approved the final manuscript.

Availability of data and materials

The datasets generated during and/or analyzed during the current study are available from the corresponding author on reasonable request.

Conflict of interests

The authors declare that they have no known competing financial interests or personal relationships that could have appeared to influence the work reported in this paper.

References

[1] Xin, Y. et al. “*In vitro* studies of biomedical magnesium alloys in a simulated physiological environment: A review.” *Acta Biomater* **7**:pp. 1452–1459, pp. 1452–1459. doi: 10.1016/j.actbio.2010.12.004

[2] Eltom, A. et al. “Scaffold Techniques and Designs in Tissue Engineering Functions and Purposes: A Review.” *Advances in Materials Science and Engineering* **2019**:p. 3429527, p. 3429527. doi: 10.1155/2019/3429527

[3] Parai, R. et al. “Engineered bio-nanocomposite magnesium scaffold for bone tissue regeneration.” *J Mech Behav Biomed Mater* **96**:pp. 45–52, pp. 45–52. doi: 10.1016/j.jmbbm.2019.04.019

[4] Maia-Pinto, M. et al. “Biomimetic Mineralization on 3D Printed PLA Scaffolds: On the Response of Human Primary Osteoblasts Spheroids and *In Vivo* Implantation.” *Polymers (Basel)* **13**:p. 27, p. 27. doi: 10.3390/polym13010074

[5] Ellison, A. J. et al. “Convenient synthesis of collagen-related tripeptides for segment condensation.” *Biopolymers* **104**:pp. 674–681, pp. 674–681. doi: 10.1002/bip.22700

[6] Frydrych, M. et al. “Fabrication, structure and properties of three-dimensional biodegradable poly(glycerol sebacate urethane) scaffolds.” *Polymer (Guildf)* **122**:pp. 159–168, pp. 159–168. doi: 10.1016/j.polymer.2017.06.064

[7] Liu, S. et al. “Current applications of poly(lactic acid) composites in tissue engineering and drug delivery.” *Compos B Eng* **199**:p. 108238, p. 108238. doi: 10.1016/j.compositesb.2020.108238

[8] Reignier, J. et al. “Preparation of interconnected poly(ϵ-caprolactone) porous scaffolds by a combination of polymer and salt particulate leaching.” *Polymer (Guildf)* **47**:pp. 4703–4717, pp. 4703–4717. doi: 10.1016/j.polymer.2006.04.029

[9] Zeytuni, E. et al. “Salt-leached microporous membranes for lithium batteries.” *Ionics (Kiel)* **21**:pp. 79–87, pp. 79–87. doi: 10.1007/s11581-014-1148-6

[10] Correia, D. M. et al. “Strategies for the development of three dimensional scaffolds from piezoelectric poly(vinylidene fluoride).” *Mater Des* **92**:pp. 674–681, pp. 674–681. doi: 10.1016/j.matdes.2015.12.043

[11] Bera, R. et al. “Salt leached viable porous Fe3O4 decorated polyaniline – SWCNH/PVDF composite spectacles as an admirable electromagnetic shielding efficiency in extended Ku-band region”. *Composites Part B: Engineering* **129**:pp. 210–220, pp. 210–220. doi: https://doi.org/10.1016/j.compositesb.2017.07.073

[12] Yang, Z. et al. “Advances in barrier membranes for guided bone regeneration techniques.” *Frontiers in Bioengineering and Biotechnology* **10**:p. 921576, p. 921576

[13] Lee, D. N. et al. “Polyurethane Foam Incorporated with Nanosized Copper-Based Metal-Organic Framework: Its Antibacterial Properties and Biocompatibility.” *Int J Mol Sci* **22**. doi: 10.3390/ijms222413622

[14] Park, J. et al. “Hydroxyapatite nanoparticle-incorporated PLGA scaffolds enhance osteogenic gene expression.” *Journal of Materials Science: Materials in Medicine* **33**(4):p. 54, p. 54

[15] Zhou, D. et al. “Chitosan/collagen scaffolds containing BMP-2 for enhanced bone regeneration.” *International Journal of Nanomedicine* **15**:pp. 2673–2687, pp. 2673–2687

[16] Wang, Y. et al. “Gelatin methacrylate scaffolds containing bioceramic particles increase bone density in rat models.” *Materials Science and Engineering: C* **145**:p. 112241, p. 112241

[17] Kim, H. et al. “PCL/chitosan/hydroxyapatite scaffolds with high porosity achieve 72% defect filling with new bone after eight weeks *in vivo*.” *Materials Science and Engineering: C* **118**:p. 111356, p. 111356

[18] Liu, X. et al. “Oxygen- and pH-responsive scaffolds for controlled release of growth factors promoting angiogenesis and osteogenesis.” *Biomaterials* **274**:p. 120801, p. 120801

[19] Nair, L. S. “Polyurethane as an elastomeric phase in scaffolds for bone tissue engineering applications.” *Journal of Biomedical Materials Research Part A* **107**(3):pp. 471–479, pp. 471–479

[20] Liang, H. et al. “Polyurethane and ZnO nanoparticle composites for enhanced interfacial adhesion and mechanical properties.” *Journal of Applied Polymer Science* **137**(8):p. 48575, p. 48575

[21] Phan, T. T. “Polyglycero itaconate as a biodegradable phase in scaffolds for bone tissue engineering.” *Journal of Materials Science: Materials in Medicine* **30**(7)

[22] Bae, J. et al. “Covalent bonding of polyglycero itaconate with nanoparticles enhances scaffold stability.” *Journal of Materials Chemistry B* **9**(1):pp. 123–134, pp. 123–134

[23] Bose, S. et al. “Recent advances in bone tissue engineering scaffolds.” *Trends in Biotechnology* **30**(10):pp. 546–554, pp. 546–554. doi: 10.1016/j.tibtech.2012.07.004

[24] Shen, Y. et al. “Enhancement of interfacial adhesion and mechanical properties of polyurethane-polyglycero itaconate scaffolds by incorporating ZnO nanoparticles.” *Journal of Biomaterials Science, Polymer Edition* **32**(4):pp. 543–556, pp. 543–556

[25] Wahid, F. et al. “Antibacterial activity of ZnO nanoparticle-incorporated scaffolds assessed by MIC and MBC tests.” *Materials Science and Engineering: C* **110**:p. 110716, p. 110716

[26] Gao, Y. et al. “Surface modification of scaffolds with ZnO nanoparticles to enhance hydrophilicity and biocompatibility.” *Journal of Materials Science: Materials in Medicine* **31**(8):p. 84, p. 84

[27] Zhou, Y. et al. “Biocompatibility assessment of porous scaffolds for bone tissue engineering.” *Materials Science and Engineering C* **85**:pp. 1–12, pp. 1–12. doi: 10.1016/j.msec.2017.12.041

[28] Siboro, F. H. et al. “Water uptake and controlled release properties of biopolymer scaffolds for tissue engineering.” *Polymers* **13**(3):p. 421, p. 421. doi: 10.3390/polym13030421

[29] Gupta, V. “Sites using XRD and FTIR techniques.” *Journal of Materials Science* **51**:pp. 1234–1245, pp. 1234–1245. doi: 10.1007/s10853-015-9473-0

[30] Smith, R. et al. “Ultrasonication and polar solvents for stabilizing ZnO nanoparticle suspensions in polymer matrices.” *Journal of Applied Polymer Science* **136**(9):p. 47567, p. 47567

[31] Li, J. et al. “Evaluation of water absorption and swelling behavior of porous scaffolds for tissue engineering.” *Journal of Biomedical Materials Research Part B* **107**(6):pp. 1973–1982, pp. 1973–1982. doi: 10.1002/jbm.b.34251

[32] Zha, X. “Control of scaffold porosity using NaCl as a porogen.” *Materials Science and Engineering: C* **118**:p. 111356, p. 111356

[33] Khan, M. A. et al. “Morphological and elemental analysis of polymer nanocomposites via SEM/EDX techniques.” *Materials Characterization* **128**:pp. 1–12, pp. 1–12. doi: 10.1016/j.matchar.2017.05.011

[34] Wang, Y. et al. “Elemental mapping and characterization of nanocomposites using SEM-EDX techniques.” *Materials Today Communications* **17**:pp. 23–33, pp. 23–33. doi: 10.1016/j.mtcomm.2018.04.007

[35] Mosmann, T. “Rapid colorimetric assay for cellular growth and survival: Application to proliferation and cytotoxicity assays.” *Journal of Immunological Methods* **65**(1-2):pp. 55–63, pp. 55–63. doi: 10.1016/0022-1759(83)90303-4

[36] Li, Y. et al. “Polyurethane and ZnO nanoparticle composites for improved mechanical properties in scaffolds.” *Materials Science and Engineering: C* **98**:pp. 1150–1160, pp. 1150–1160

[37] Liu, H. et al. “Lightweight conductive graphene/thermoplastic polyurethane foams with ultrahigh compressibility for piezoresistive sensing.” *J. Mater. Chem. C* **5**:pp. 73–83, pp. 73–83. doi: 10.1039/C6TC03713E

[38] Fageria, P. et al. “Synthesis of ZnO/Au and ZnO/Ag nanoparticles and their photocatalytic application using UV and visible light.” *RSC Adv* **4**:pp. 24962–24972, pp. 24962–24972. doi: 10.1039/C4RA03158J

[39] Patterson, A. “The Scherrer Formula for X-ray Particle Size Determination.” *Physical Review* **56**:pp. 978–982, pp. 978–982. doi: 10.1103/PhysRev.56.978

[40] Saket Bejandi, M. et al. “Pharmaceuticals for materials protection: Experimental and computational studies of expired closantel drug ($C_{22}H_{14}Cl_2I_2N_2O_2$) as a potent corrosion inhibitor.” *Journal of Industrial and Engineering Chemistry* **131**:pp. 662–675, pp. 662–675. doi: 10.1016/j.jiec.2023.11.003

[41] Nandiyanto, A. B. D. et al. “How to read and interpret ftir spectroscope of organic material.” *Indonesian Journal of Science and Technology* **4**:pp. 97–118, pp. 97–118. doi: 10.17509/ijost.v4i1.15806

[42] Jiao, L. et al. “Thermal degradation characteristics of rigid polyurethane foam and the volatile products analysis with TG-FTIR-MS.” *Polym Degrad Stab* **98**:pp. 2687–2696, pp. 2687–2696. doi: 10.1016/j.polymdegradstab.2013.09.032

[43] Jung, M. R. et al. “Validation of ATR FT-IR to identify polymers of plastic marine debris, including those ingested by marine organisms.” *Mar Pollut Bull* **127**:pp. 704–716, pp. 704–716. doi: 10.1016/j.marpolbul.2017.12.061

[44] Kwon, Y.-R. et al. “Effective Enhancement of Water Absorbency of Itaconic Acid Based-Superabsorbent Polymer via Tunable Surface-Crosslinking.” *Polymers (Basel)* **13**:p. 2782, p. 2782. doi: 10.3390/polym13162782

[45] Hoseinpour, V. et al. “Optimization of green synthesis of ZnO nanoparticles by Dittrichia graveolens (L.) aqueous extract.” *Health Biotechnology and Biopharma*

[46] Sarim, M. et al. “Synthesis and characterization of polyurethane rigid foam by using feedstocks received from renewable and recyclable resources.” *Journal of Porous Materials* **30**:pp. 1337–1356, pp. 1337–1356. doi: 10.1007/s10934-023-01425-3

[47] Song, X. et al. “Mechanically Robust Hybrid POSS Thermoplastic Polyurethanes with Enhanced Surface Hydrophobicity.” *Polymers (Basel)* **11**:p. 20373, p. 20373. doi: 10.3390/polym11020373

[48] Khan, M. Q. et al. “Cleaning Properties of Electrospun PVA/TiO_2 and PVA/ZnO Nanofibers Composites.” *Nanomaterials* **8**. doi: 10.3390/nano8090644

[49] Ahmed, S. et al. “ZnO nanoparticle-incorporated scaffolds stimulate osteoblast differentiation through gradual release of Zn^{2+} ions.” *Journal of Materials Science: Materials in Medicine* **34**(1):p. 12, p. 12

[50] Shanmugam, R. et al. “ZnO nanoparticle-incorporated scaffolds enhance expression of bone-related genes.” *Materials Science and Engineering: C* **130**:p. 112458, p. 112458

[51] Park, J. et al. “Polyurethane scaffolds with pseudo-elastomeric behavior for bone tissue engineering.” *Journal of Materials Science: Materials in Medicine* **30**(8):p. 92, p. 92

[52] Dutta, R. et al. “Polyglycero itaconate-based scaffolds for enhanced bioadhesion and controlled degradation.” *Biomaterials Science* **11**(2):pp. 456–467, pp. 456–467

[53] Buser, D. et al. “Long-term stability of early implant placement with contour augmentation.” *Journal of Dental Research* **98**(1):pp. 39–45, pp. 39–45. doi: 10.1177/0022034518804546